Intermetallics 143 (2022) 107495

Contents lists available at ScienceDirect

Intermetallics

journal homepage: www.elsevier.com/locate/intermet

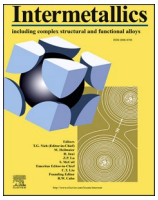

Synthesis, microstructure, and thermoelectric properties of Sb-Based high entropy alloys

Jamil Ur Rahman [a], Patricia Almeida Carvalho [b], Nayereh Soltani [a], Matthias Schrade [b], Anette Eleonora Gunnaes [a], Terje G. Finstad [a,*]

[a] Department of Physics, Centre for Materials Science and Nanotechnology, University of Oslo, 0371, Oslo, Norway
[b] SINTEF Materials and Chemistry, 0373, Oslo, Norway

ARTICLE INFO

Keywords:
Sb-Based high entropy alloys
Intermetallics
Thermoelectric materials
Lattice thermal conductivity

ABSTRACT

In this paper, we explore the synthesis of new antimonide compounds based upon concepts of high entropy alloys (HEA). HEAs are usually multi-element ($\gtrsim$5) alloys with near the equiatomic composition. They have been given very large attention due to their vast potential within many fields. We investigated the thermoelectric transport properties of antimony-based high entropy alloys. The observed electrical conductivity, Seebeck coefficient, and thermal conductivity were comparable to those of cutting-edge half-Heusler thermoelectric alloys. Alloys with different valence electron counts (VEC) were synthesized and correlated with measured electrical properties.

1. Introduction

Thermoelectric (TE) technology serves to directly transform a heat flux into useful electric power. The efficiency of a TE material is specified by its dimensionless figure of merit (zT), which can be expressed as $zT = S^2\sigma/\kappa T$, where S represents the Seebeck coefficient, σ is the electrical conductivity, κ is the total thermal conductivity, and T is the absolute temperature [1,2]. To obtain a high zT value the material must have high values of S and σ combined with a low value for κ. The κ has contributions from electrons and phonons and is written as $\kappa = \kappa_e + \kappa_L$. Here κ_e and κ_L are the electronic thermal conductivity and the lattice thermal conductivity, respectively. To optimize for a high zT, the ratio $\sigma/(\kappa_e+\kappa_L)$ should be maximized, while σ and κ_e are dependent through the Wiedemann-Franz law $\kappa_e = L\sigma T$, where L is the Lorenz number/-function [3–6]. For low values of σ, zT will increase with increasing σ but will decrease for high values of σ since κ_e then increase with σ. So, careful optimization is needed to improve the zT value. Many efforts have been made in zT enhancements through κ_L reduction using nanostructuring [7], nanocomposites [8], and inclusions [9], while for the best performing TE materials, the value of κ_L is at the phonon-glass limit [2], which is a fundamental lower limit.

Over the past decades, there has been a large interest in intermetallic compounds belonging to the family of Heusler compounds having simple crystal structures [10,11]. The attractive features are: diverse electrical properties, thermal stability, and mechanical robustness. Heusler compounds are promising functional materials for many application areas including spintronics [12,13], thermoelectrics [14–19], topological insulators [20,21], optoelectronics [22,23], and solar cells [24,25]. A bottleneck for TE applications of the simple half-Heusler compounds has been their large κ_L and there are many reports on attempts to minimize it [26–28]. Among the approaches has been substituting atoms to increase the disorder to approach the phonon glass limit, and introducing precipitates and grain boundaries to increase phonon scattering.

HEA are multi-element ($\gtrsim$5) alloys with near equiatomic composition. They have been given large attention due to their vast potential within many fields [29,30]. One driving force behind the vastly increasing volume of research reports on HEA-materials has been to investigate the unexplored central region of the multi-component alloy phase space. A simple explanation for the structure of HEAs is that high configurational entropy may thermodynamically favor the single solid solution phases over alloys with intermetallic (IM) phases [31]. The high configurational entropy may in general extend the phase space that is available for exploring new materials, which may lead to the discovery of the materials that are needed for a sustainable future. The concepts for HEA alloys can be transferred to research on compounds, which are not necessarily metallic. Here, we call it HEA-based compounds, which have also been suggested to have many interesting structural and functional properties [29–34]. In addition, the complex phase of these alloys can be a success factor for the cases where inharmonicity and nanostructuring are beneficial [35,36]. The high degree of disorder on

* Corresponding author.
E-mail address: terje.finstad@fys.uio.no (T.G. Finstad).

https://doi.org/10.1016/j.intermet.2022.107495
Received 15 November 2021; Received in revised form 25 January 2022; Accepted 5 February 2022
Available online 15 February 2022

some of the sublattices of HEAs may increase the phonon scattering and is thus conceptually similar to thermal conductivity reduction strategies in research on thermoelectric materials, as mentioned above. Thus, it is rational to speculate that the extreme chemical disorder in HEAs could possibly retain low lattice thermal conductivity resulting from their strong inharmonicity, and thus may open the door for new and unexplored avenues of HEAs as next-generation materials. High TE performance has been reported in PbSe and $SnSe_3$ based HEAs [37,38]. However, the use of toxic and expensive elements restricts its use for practical applications. Thus it is important to search for the compounds that are composed of earth-abundant elements and have an environmentally friendly nature. Amongst them, antimonides based intermetallic compounds are considered the best due to their environmentally friendly, earth-abundant, excellent stability, and potential for applications in various fields e.g., thermoelectrics [39,40], batteries [41,42], electrocatalytic activity in hydrogen evolution reaction [43], catalytic activity in hydrogenation [44], etc. For TE applications, much of the attention has been drawn to Sb-based compounds like half-Heusler [45,46], clathrates [47], zintl-antimonides [48], and skutterudites [49,50]. However, the concept of realizing HEA in Sb-based compounds is largely ignored and needs special attention to explore this avenue for TE applications.

We tackle the challenge of employing Sb-based HEAs as next-generation materials by using the conventional flame melting technique for preparing antimonide-based compounds starting by replacing the binary promising TE (ZnSb) [51] with an alloy having 5 elements at the Zn site, i.e., $Zn_{1-a-b-c-d-e}Sb$, where a = Zn, b = Fe, c = Co, d = Ni, and e = Mn. After melting the compound, it is segregated into a mixture of different phases. The compositions of each phase in a multiphase alloy were observed by scanning electron microscopy (SEM) coupled with energy dispersion spectroscopy (EDS) capabilities. An alloy having large volume fraction composition that satisfies the conditions of HEAs both by compositions-based and by calculated configurational entropy was selected and synthesized for further investigations. Fortunately, the resulting single-phase materials adopt a Heusler type structure, which is an interesting material for TE applications. Heusler-like alloys are flexible to adapt their physical properties by simply changing the number of Valence Electron Counts (VEC) present. For example, the known semiconductors are alloys with VEC = 8 or 18 [12]. Therefore, we calculate the VEC of the crystallized alloy by assuming a solid solution of $(MnNiSb)_{1-x}(ZnFe_{1-y}Co_ySb)_x$, where $x = 0.33$ and $y = 0.55$ and found that the final skimmed $Zn_{16.67}Fe_{9.17}Co_{7.5}Ni_{16.67}Mn_{16.67}Sb_{33.33}$ alloy have a VEC = 18.72. Then, we adjusted the alloys according to the VEC rule, and a new set of alloys $Zn_{20.3}Fe_{11.2}Co_{9.15}Ni_{13}Mn_{13}Sb_{33.33}$ (VEC = 18) and $Zn_{25.4}Fe_{14}Co_{11.5}Ni_{7.9}Mn_{7.9}Sb_{33.33}$ (VEC = 17) were synthesized1 and their thermoelectric properties were examined. The subsequent samples were denoted with the prefix VEC = 18.72, VEC = 18, and VEC = 17 respectively.

2. Experimental methods

First, for the synthesis of $Zn_{10}Fe_{10}Co_{10}Ni_{10}Mn_{10}Sb_{50}$ alloy, high-purity elemental Zn (99.99%) shot, Fe (99.99%) wire, Co (99.95%) granule, Ni (99.95%) wire, Mn (99.95%) flake, and Sb (99.99%) ingots were used as a starting material. The nominal compositions were weighed according to the stoichiometry and sealed in an evacuated thick-walled quartz ampule. The evacuated quartz ampoule was then heated using the flame melting technique and cooled in water before annealing. Care was taken to ensure complete melting and the homogeneity of the alloys. Individual phase compositions in a multiphase alloy were examined by scanning electron microscopy (SEM) coupled with energy dispersion spectroscopy (EDS) capabilities. Based on the results of the EDS, alloys with the new compositions were prepared. Since the overall composition was confirmed as an effective additional standard within the expected error limits, the individual phase compositions in multi-phase alloys could be determined with confidence. The structural characterization of the selected alloys was done by X-ray diffraction (XRD), using Bruker D8 discover with Cu Kα. For thermoelectric properties measurement selected alloys were ground into powder and then hot-pressed into pellets at 973 K for 30 min. The temperature dependence electrical properties were measured using the custom-designed setup [52]. The room temperature Hall mobility and carrier concentration was measured with the sample in the van der Pauw pattern. The thermal conductivity was measured by the laser flash method using a Netzsch LFA457.

3. Results and discussions

The equilibrated microstructure of the as-cast $Zn_{10}Fe_{10}Co_{10}Ni_{10}Mn_{10}Sb_{50}$ alloy is shown in Fig. 1(a), which exhibits the co-existence of three different phases having different shades of grey (bright-medium-dark). The phase distribution in the as-cast alloys is relatively fine and with diffuse phase boundaries. To verify the compositions of each phase, elemental analysis was performed with energy-dispersive X-ray spectroscopy (EDS). According to EDS analysis, the first phase, with a medium grey appearance in the SEM and a large volume fraction has an approximate composition of $Zn_4Fe_{15}Co_{15}Ni_{13}Mn_5Sb_{48}$. The second phase, with a dark grey color and a small volume fraction, has a composition of $Zn_{14}Fe_6Co_{10}Ni_{14}Mn_{16}Sb_{40}$. The third phase, with bright grey color, has an approximate composition of $Zn_4Fe_{14}Co_{12}Ni_{10}Mn_5Sb_{56}$. However, after the heat treatment at 550 °C for 20 h, there are still three different regions, each with the same shade of grey as before, but the volume proportions have changed as seen in Fig. 1(b). The first phase (medium grey) has changed the composition marginally to approximately $Zn_4Fe_{14}Co_{15}Ni_{14}Mn_4Sb_{47}$ but its volume fraction was reduced. Moreover, the second phase (dark grey) has changed composition marginally to $Zn_{16}Fe_{10}Co_8Ni_{13}Mn_{15}Sb_{39}$ and its volume fraction has increased. The third phase (bright grey) has also increased its volume fraction and changed composition marginally to $Zn_2Fe_{12}Co_{17}Ni_5Mn_4Sb_{60}$. It can be seen that the amount of the first phase (medium grey) with a large volume fraction in the as-cast state is reduced significantly after the heat treatments and some of it transforms into the second phase (dark grey) as shown in Fig. 1(b). This suggests that this medium grey phase is metastable and retained only when quenched with water. Fig. 1(c) is the EDS elemental mapping of the heat-treated surface showing a clear distribution of the two major phases.

Boltzmann's equation for a system can realize its state with equal probability if the atoms are interchanged will have a configurational entropy of mixing per mole given by equation (1):

$$\Delta S_{mix}^{conf} = RlnW \tag{1}$$

where R is the universal gas constant (8.314 J/K mol) and W is the number of different ways of arranging the atoms in the system/solution. The total mixing entropy ΔS_{mix}, can be divided into four contributions as shown in equation (2):

$$\Delta S_{mix} = \Delta S_{mix}^{vib} + \Delta S_{mix}^{mag} + \Delta S_{mix}^{elec} + \Delta S_{mix}^{conf} \tag{2}$$

Here ΔS_{mix}^{vib} is the vibrational entropy, ΔS_{mix}^{mag} is the magnetic dipole entropy, ΔS_{mix}^{elec} is the electronic randomness entropy, and ΔS_{mix}^{conf} is the configurational entropy. Here we only consider the configurational entropy, as the relative difference in this term will be the satisfactory yardstick for comparing the potential complexity of various alloy compositions, and the other terms cannot presently be calculated with confidence [53]. For an ideal random n-component solid solution, its configurational entropy of mixing per mole is given by equation (3) [29]:

$$\Delta S_{conf} = -R(x_1 lnx_1 + ... + x_n lnx_n) \tag{3}$$

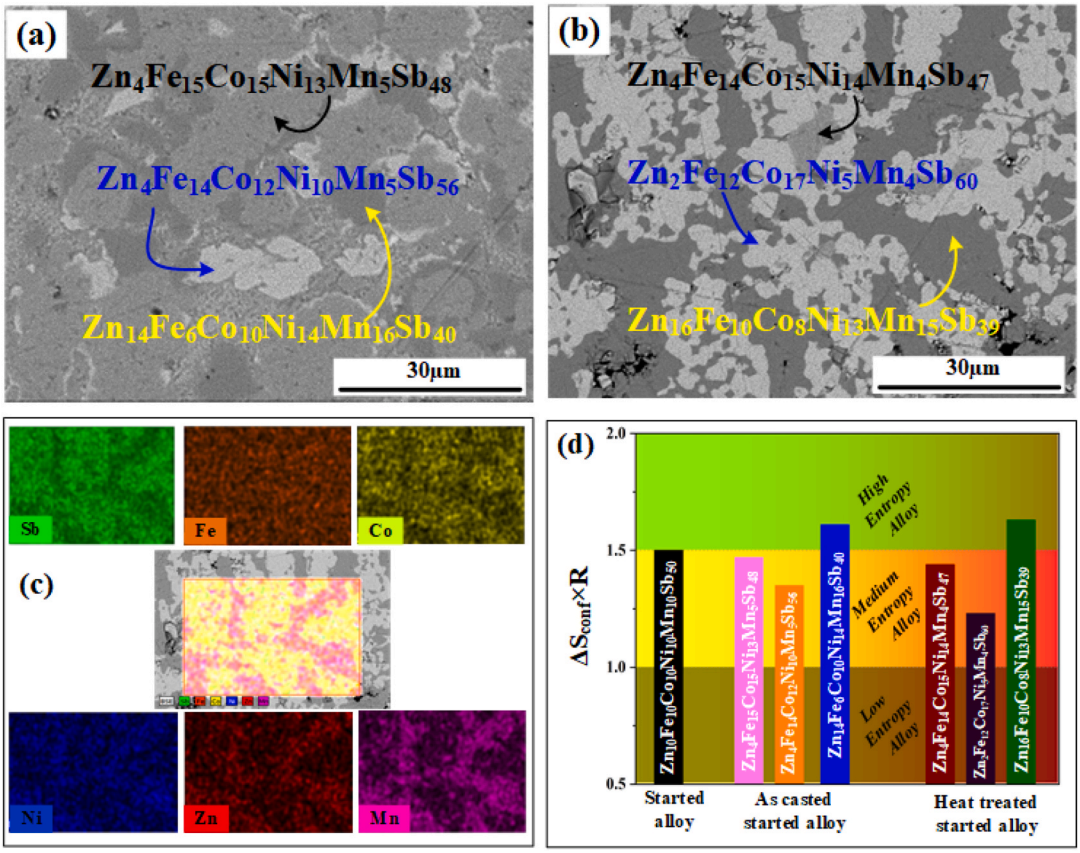

Fig. 1. SEM images of $Zn_{10}Fe_{10}Co_{10}Ni_{10}Mn_{10}Sb_{50}$ (a) as-cast and (b) heat-treated (550 °C for 20 h) (c) EDS results of heat-treated alloys.

$$\Delta S_{conf} = -R\sum_{i=1}^{n} x_i ln x_i \quad (4)$$

where x_i is the mole fraction of the i-th element, and n is the number of the components. Configurational entropy values have been used to classify materials as high-entropy alloys (>1.5 R), medium entropy alloys (MEAs) (1–1.5 R), and low entropy alloys (LEAs) (<1 R) [54]. Considering the starting composition, $Zn_{10}Fe_{10}Co_{10}Ni_{10}Mn_{10}Sb_{50}$, the calculated configurational for a solid solution entropy is 1.5 R, which is the boundary line between HEAs and MEAs. As seen from the EDS data, after the melting and annealing the alloy exhibits the co-existence of three different phases. We calculated the configurational entropy for each composition and the results are presented in Fig. 1(d). The composition $Zn_{16}Fe_{10}Co_8Ni_{13}Mn_{15}Sb_{39}$ has a configurational entropy of 1.61 R. It is the composition of the dark grey phase in Fig. 1(b) having increased volume fraction with annealing and therefore indicating stability. This composition satisfies the conditions of HEAs both by compositions-based and by calculated configurational entropy. Hence, further investigations were concentrated on exploring the $Zn_{16}Fe_{10}Co_8Ni_{13}Mn_{15}Sb_{39}$ phase. Even if one can assign a value to a composition, it should be clear that one could not determine the entropy of the phase before knowing the ordering of the atoms. For compounds with other parameter combinations are suggested as descriptors indicating the stability of compounds [55], but the configurational entropy is important.

To explore the selected HEAs composition, $Zn_{16}Fe_{10}Co_8Ni_{13}Mn_{15}Sb_{39}$ was synthesized, and Fig. 2(a) shows the as-cast microstructures of the selected alloys. Here, we considered the as-casted alloys because there was not much difference between the as-casted and the heat-treated alloy (550 °C 20 h). To characterize the compositions of the different phases, at least 10 EDS points at different places were used and the variations in the compositions were equal within the uncertainty. The chemical composition (in at. %) of the three phases is characterized by EDS and is shown in Fig. 2(a). The solidification of $Zn_{16}Fe_{10}Co_8Ni_{13}Mn_{15}Sb_{39}$ yields segregation into a phase with the composition, $Zn_{16}Fe_{10}Co_8Ni_{15}Mn_{17}Sb_{35}$, and a small volume fraction of other phases. The separation into different phases is seen more clearly by the elemental mapping with EDS as shown in Fig. 2(c). It can be seen that Zn, Mn, and Sb segregate towards the minor phases, while Ni, Fe, and Co have an almost homogenous distribution. The corresponding XRD pattern also tells that the selected alloy stabilizes in a three-phase region. Following the calculation of configurational entropy approaches, as described above equation (4), the ΔS_{conf} of the new compositions were calculated and presented in Fig. 2(d). One of the three phases has the compositions of HEA and the calculated ΔS_{conf} is in the HEA regions. Interestingly, the stoichiometry of this HEA indicates a Heusler type structure. Therefore, an alloy with a composition close to $Zn_{16.67}Fe_{9.17}Co_{7.5}Ni_{16.67}Mn_{16.67}Sb_{33.33}$, which was considered as a hypothetic solid solution in a Heusler structure, was synthesized and the microstructure is shown in Fig. 2(b). This alloy is a single-phase and its crystal structure matches a Heusler type [18]. The EDS element mapping confirmed a uniform distribution of all elements (Not shown here). We consider the phase to have an XYZ half-Heusler type composition, where Sb occupies the Z site in a NaCl sublattice, which is reasonable since Sb is the most electronegative element in the phase and occupies 1/3 of the sites. The other five elements would then substitute for X and Y in the Heusler composition. We may consider this as a "high entropy version". It can be viewed as a solid solution consisting of $(MnNiSb)_{1-x}(ZnFe_{1-y}Co_ySb)_x$ where $x = 0.33$ and $y = 0.55$. Likewise, it can be viewed as a solid solution of three ternary compounds: MnNiSb, ZnFeSb, and ZnCoSb. Here, MnNiSb is a half-metallic ferromagnet [56–58] with the half-Heusler-structure ($C1_b$, $F\bar{4}3m$, #216) having a bandgap for minority spins, while no gap for majority spins. ZnFeSb has been reported to be a stable compound with a half-Heusler crystal structure ($C1_b$, $F\bar{4}3m$, #

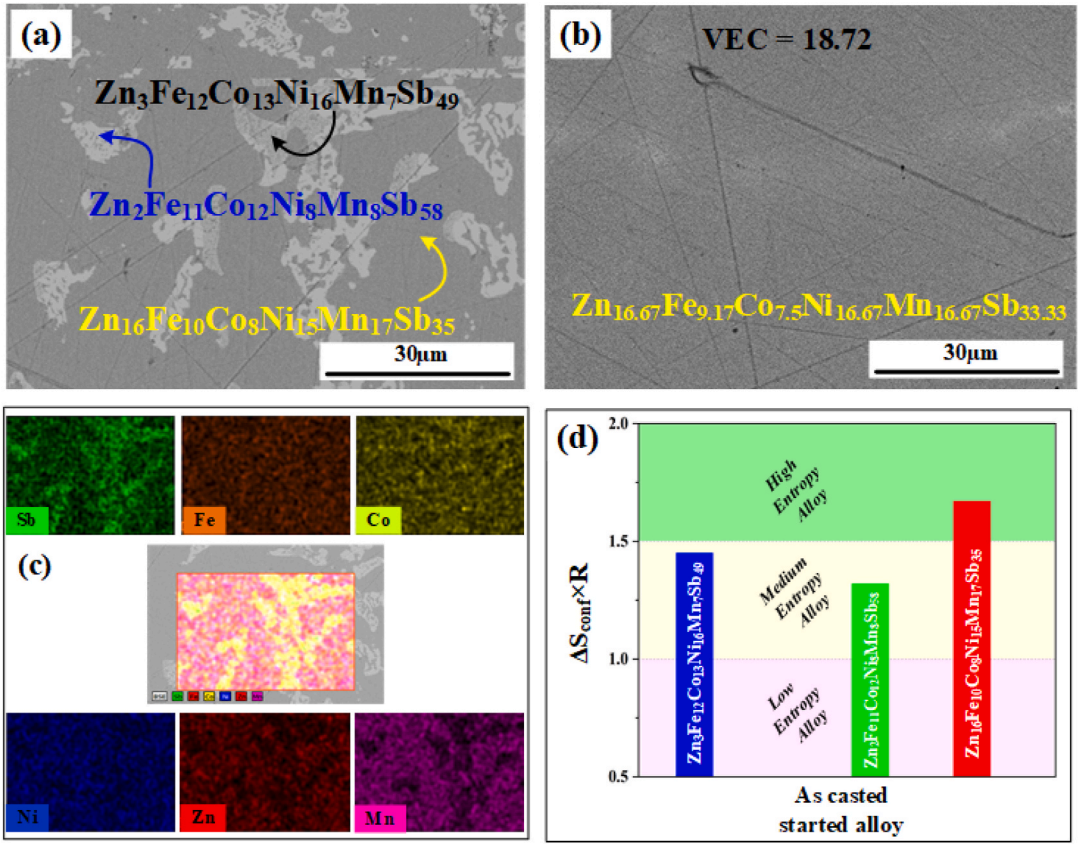

Fig. 2. (a) SEM image of starting composition $Zn_{16}Fe_{10}Co_8Ni_{13}Mn_{15}Sb_{39}$ yielding three annotated compositions (which did not change by heat treatment) (b) SEM image of starting composition $Zn_{16.67}Fe_{9.17}Co_{7.5}Ni_{16.67}Mn_{16.67}Sb_{33.33}$ (c) EDS mapping of elements for the starting composition $Zn_{15.50}Fe_{10.19}Co_{7.70}Ni_{12.57}Mn_{14.74}Sb_{39.29}$ and (d) Entropy of mixing "yard sticks" for selected compositions.

216). Chumak et al. reported that the ZnFeSb compound crystallizes into ($C1_b$, $F\bar{4}3m$, #216) and is stable in the equilibrium ternary phase diagram at 300 °C [59]. This is in agreement with Xiong et al. [60], who in addition report a structure with a 2 × 2 × 2 supercell of a normal half-Heusler structure with a composition $Fe_{0.98}Zn_{0.84}Sb$. On the other hand, Persson [61] reports calculations indicating that this structure has an energy of 0.4 eV above the convex hull in the phase diagram (at 0 K) and would not be stable at equilibrium at low temperatures. For the ZnCoSb system Xiong et al. [62] list a 2 × 2 × 2 supercell of half-Heusler structure, yielding symmetry of ($Fm\bar{3}m$) and having a composition of $Co_8Zn_8Sb_8$. This indicates that the observation of a Heusler type structure for $Zn_{16.67}Fe_{9.17}Co_{7.5}Ni_{16.67}Mn_{16.67}Sb_{33.33}$ is reasonable, but not obvious.

It should be noted that most of the known semiconductor-like Half-Heusler (HH) alloys have a VEC of 18 [63]. The calculated VEC for the $Zn_{16.67}Fe_{9.17}Co_{7.5}Ni_{16.67}Mn_{16.67}Sb_{33.33}$ alloy is 18.72. To probe the effect of adjusting the VEC and its impact on the TE properties new alloys with VEC 18 and 17 have been prepared as shown in Fig. 3(a) and (b). The as-casted alloy with different VEC also shows a single-phase region without any agglomerations. The configurational entropy of alloys with different VEC was also calculated. As the stoichiometry and XRD indicate a HH type structure, therefore, we comment briefly on the configurational entropy of the compounds knowing that they are Heusler type alloys with a stoichiometry that is HH-like. We look at three simple possibilities. One is that we have sub-lattices XYZ, where Sb is occupying the Z lattice and does not contribute to configurational entropy, while the other elements are occupying randomly X and Y sites. Base on this assumption, the calculated configurational entropy is shown in Fig. 3(c). It is interesting to see that upon moving away from VEC 18.72 to 17, these alloys remain single-phase HEAs in the sense of containing 5 to 40 at.% of each element. But the alloy with VEC 17 lies at the boundary line between HEAs and MEAs. Another possibility is that we have the sublattices X_1X_2YZ and that we have as many vacancies as we have Sb atoms. If all the vacancies were positioned on the X_1 sublattice then we would have the first case. But if we make a case where the vacancies occupy X_1, X_2, and Y with equal probability, as do the other elements except Sb, which occupies the Z sublattice then, the configurational entropy of all VEC alloys is 2.0 R. While for the third possibility, we get an entropy of mixing equal to 1.9 R by considering the $Co_8Mn_8Sb_8$ structure, which consists of 8 layers of "Mn–Sb" and 8 layers of "Co & Vacancy" layers. We let the Mn site vary randomly with Mn and Zn while the "Co & Vacancy" layer varies with Co, Fe, and vacancies. The elemental mapping (Fig. 3(d)) confirmed that all elements reveal a homogenous distribution. The five elements in the $X(X_1X_2)$ and Y sublattice have large configurational entropy that could contribute to the formation of a single-phase, and the enhanced synthesizability compared to simple HH compounds. To check the homogeneity of the compositions, 5 EDS point measurements were carried out in different places and the results are presented in Table 1. It is interesting to see that the variation in the stoichiometry at different locations is almost the same and close to the nominal compositions. We also calculate the VEC of the actual compounds, based upon the observed EDS results. It suggests that the VEC of the actual compounds deviate from the nominal VEC, which was calculated. This is connected to the evaporation of elements with high vapor pressure during the alloying of the compound.

Fig. 4 shows the X-ray diffraction patterns of samples containing various nominal VEC (18.72, 18, and 17). All peaks correspond to the Heusler-type structure $Co_8Mn_8Sb_8$ [64–66], which has the regular HH peaks and additional peaks (indicated by arrows) from the symmetry breaking of the 2 × 2 × 2 supercell. This proposes that all samples crystallize in a structure of 2 × 2 × 2 supercell of normal Heusler type

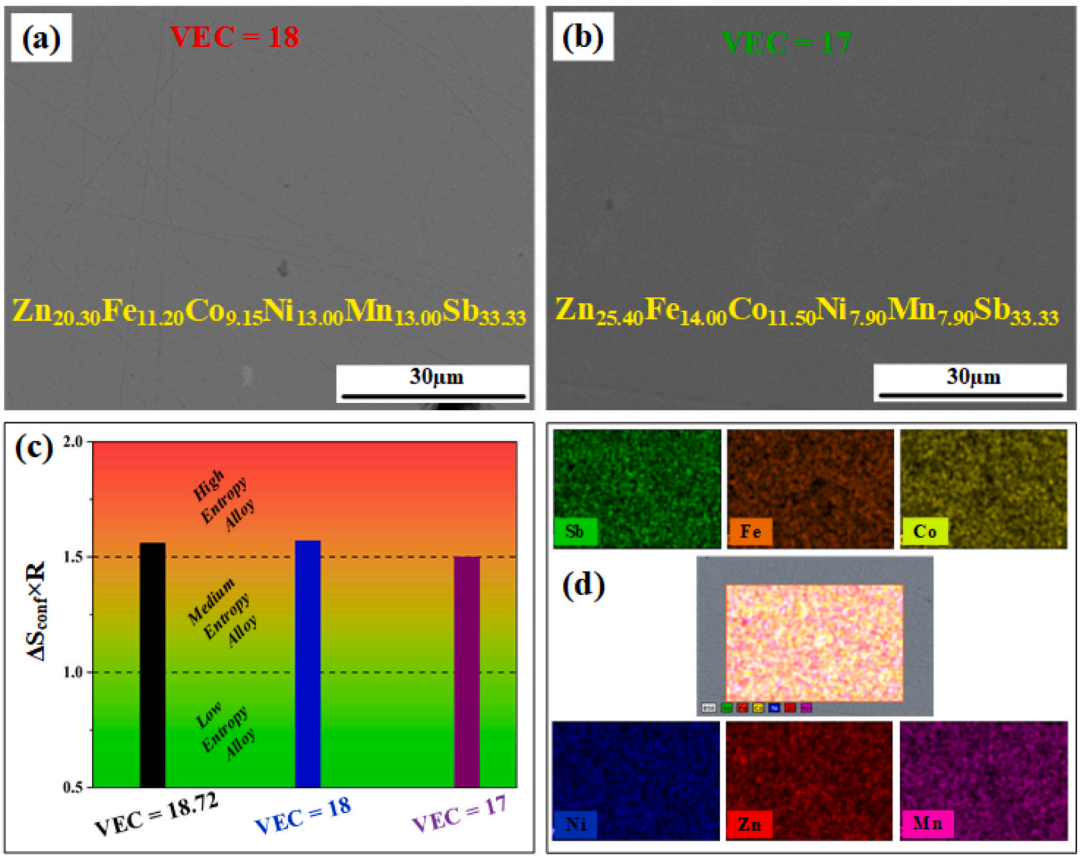

Fig. 3. (a) and (b) SEM images of the as-casted for VEC = 18 and 17, (c) Entropy of mixing "yard sticks" for various VEC alloys, and (d) EDS results of VEC = 18 alloys.

Table 1
Chemical compositions of VEC = 18.72, 18, and 17 alloys as obtained by SEM-EDS.

$Zn_{16.67}Fe_{9.17}Co_{7.50}Ni_{16.67}Mn_{16.67}Sb_{33.33}$ → (VEC-18.72)						
EDS result	Zn (at. %)	Fe (at. %)	Co (at. %)	Ni (at. %)	Mn (at. %)	Sb (at. %)
area-1	15	10	7	16	18	34
area-2	13	9	8	17	19	34
area-3	15	9	9	17	17	33
area-4	16	10	9	17	16	33
area-5	15	9	8	18	16	34
(averaged)	**15**	**9**	**8**	**17**	**17**	**34**
Averaged composition VEC → 19.03						
$Zn_{20.30}Fe_{11.20}Co_{9.15}Ni_{13.00}Mn_{13.00}Sb_{33.33}$ → (VEC-18)						
EDS result	**Zn (at. %)**	**Fe (at. %)**	**Co (at. %)**	**Ni (at. %)**	**Mn (at. %)**	**Sb (at. %)**
area-1	18	11	9	13	15	34
area-2	18	11	10	12	15	34
area-3	19	12	10	12	14	33
area-4	17	11	10	12	16	34
area-5	18	11	10	13	16	33
(averaged)	**18**	**11**	**10**	**13**	**15**	**34**
Averaged composition VEC → 18.37						
$Zn_{25.40}Fe_{14.00}Co_{11.50}Ni_{7.90}Mn_{7.90}Sb_{33.33}$ → (VEC-17)						
EDS result	**Zn (at. %)**	**Fe (at. %)**	**Co (at. %)**	**Ni (at. %)**	**Mn (at. %)**	**Sb (at. %)**
area-1	20	15	14	8	9	35
area-2	20	16	13	8	9	34
area-3	20	14	14	7	10	35
area-4	19	16	14	8	9	34
area-5	20	15	15	8	8	34
(averaged)	**20**	**15**	**14**	**8**	**9**	**34**
Averaged composition VEC → 17.97						

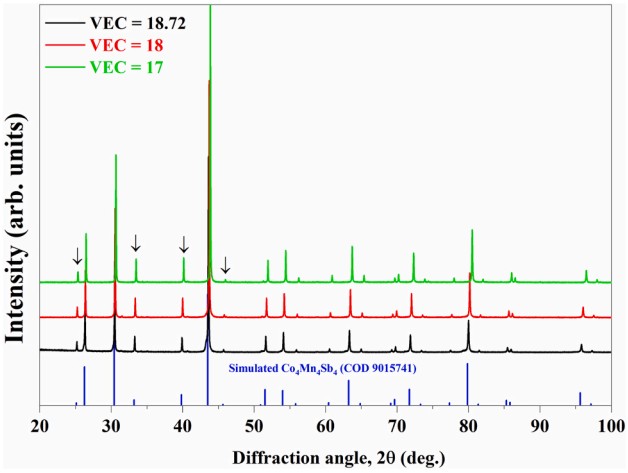

Fig. 4. XRD patterns of high entropy alloys synthesized with different nominal valence electron counts, VEC. See Table 1 for their actual concentration. All peaks agree with the Co8Mn8Sb8 pattern, which shares the pattern with NiMnSb, but has the 2 × 2 × 2 superstructure peaks in addition which are marked with an arrow.

cells similar to $Co_8Mn_8Sb_8$, where every two layers are shifted relative to the previous layer. The precise crystal structure determination using high-resolution TEM and first-principles calculations of these alloys would be reported elsewhere.

Fig. 5(a) represents the temperature-dependent electrical conductivity for samples having various VEC (18.72, 18, and 17). The value of the conductivity for all three samples is small compared to that for

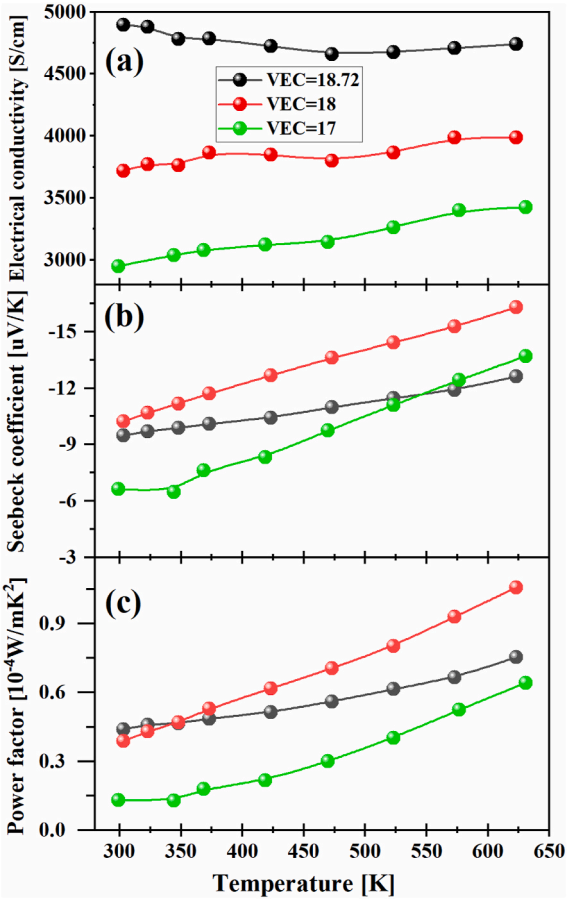

Fig. 5. Temperature-dependent (a) electrical conductivity (b) Seebeck coefficient, and (c) power factor for VEC (18.72, 18, and 17).

common metals. A substantial part of the resistivity comes from alloy scattering due to the atomic element substitutions. Alloy scattering is essentially temperature-independent. It will be different for the three samples with different VEC, due to their different disorder. The supercell structure may also have varying degrees of disorder, which will be studied further. The different VEC for the samples will also shift the Fermi level among the density of states and the effective carrier concentration will be different for the different samples. Hall measurements gave a carrier concentration of 1.57×10^{22}, 1.75×10^{21}, and 1.15×10^{21} for VEC = 18.72, 18, and 17 respectively. We see that the measured conductivity follows the same trend with VEC as that of carrier concentration, but there is probably also an influence of different transport properties among the samples with different VEC. The temperature dependence of the conductivity is different for different VEC seen in Fig. 5(a). For the sample with VEC = 18.72, the slope is negative (up to 450 °C), which is usually considered as metallic behavior. Above this transition region; a slight increase in the electrical conductivity is observed with temperature, considered as semiconducting-like behavior. For the sample with VEC = 18 and 17, the electrical conductivity is lower than that for VEC = 18.72 and the temperature derivative has a positive slope.

Fig. 5(b) represents the temperature dependence of the Seebeck coefficient. The negative values indicate that electrons dominate electrical transport properties. The absolute value of the Seebeck coefficient increases with increasing temperature irrespective of VEC, which is typical and results from more electrons around the Fermi level contributing to the transport at higher temperatures [67]. For semiconductors, it can be related to the effective density of states of the conduction band increasing with temperature. While the absolute value of the Seebeck coefficient is low, it increases slightly upon moving away from VEC = 18.72 to 18 and then decreases for VEC = 17, this point can be attributed due to a modification in the shape of the band structure near the Fermi level.

The power factor (PF) is one of the main indicators to evaluate TE performance and can be calculated from the Seebeck coefficient and electrical conductivity by $PF = \sigma \cdot S^2$ and is presented in Fig. 5(d). The value of PF increases with increasing temperature because the Seebeck coefficient increase. Thus, the resulting FP reaches a maximum value of 1.07×10^{-4} W/mK^2 at 630 K.

Given the TE performance of the compounds, not only PF but also figure-of-merit (zT) is important. To assess the zT of the compounds, we need to obtain the temperature dependence of the total thermal conductivity (κ_{tot}), which is presented in Fig. 6(a). It continuously decreases by moving the VEC from 18.72 to 17 and increases as the temperature increases. To understand the continuous decreases in κ_{tot} by moving the VEC from 18.72 to 17, we estimated the influence of κ_e and κ_L to κ_{tot} by using Wiedemann-Franz law to figure out the dominant factors [3,68]. The Lorenz number was calculated by assuming a single parabolic band and acoustic phonon scattering [9]. The calculated Lorenz numbers were in between 2.43×10^{-8} WΩK^{-2} to 2.42×10^{-8} WΩK^{-2} in the whole temperature range. The estimated κ_e and κ_L are presented in Fig. 6 (b) and (c). We can see that κ_e is about half as high as κ_{tot}, while the rest is ascribed $\kappa_L = \kappa_{tot}$-κ_e. Here, it should be noted that the decrease in κ_{tot} with decreasing VEC is due to the decrease in electrical conductivity observed in Fig. 5(a). Using the PF and κ_{tot} data, we calculated the temperature-dependent zT to predict the performance for TE application and as shown in Fig. 6(d). The sample with VEC = 17 enables $zT = 0.008$ at 630 K. The observed increasing trend with temperature indicating that higher zT is achievable at higher temperatures. Based on these results, it can be anticipated that optimizing the phonon contribution and the Seebeck coefficients left considerable room for further improvements. Consequently, all antimonides studied in this work may be considered promising materials for future exploration, especially if their electronic transport properties are optimized for TE applications.

4. Conclusion

A family of new high entropy alloys based on antimonides with Heusler-like compositions was synthesized and their thermoelectric properties explored. Due to specific structural order, these alloys exhibit a correlation between the electrical properties and the VEC of the system. By changing the VEC from 18.72 to 17 the temperature-dependent electrical conductivity changes from metal to semiconducting-like behavior. Furthermore, this decrease in VEC also decreases the total thermal conductivity, which is ascribed due to a decrease in electronic thermal conductivity. It is interesting to note that all samples have relatively low thermal conductivity compared to the state-of-the-art Half-Heusler TE alloys. These findings suggest that carefully adjusting the electrical properties could enhance the TE performance and the possibility to exploit antimonides-based High Entropy alloys with Heusler-type compositions as a new class of future TE materials. This new development in alloys could also open a new door to new alloying systems, which could be applied to various energy harvesting applications and basic research.

Author statements

J.U.R. and P.A.C initiated the concepts and designed the experiments; N.S. carried out detailed data analysis and performed calculations; M.S. measured the transport properties; A.E.G. contributed with discussion and commented on the manuscript. T.G.F. analyzed the data and lead the research work. All the authors shared ideas and contributed to the interpretation of the results.

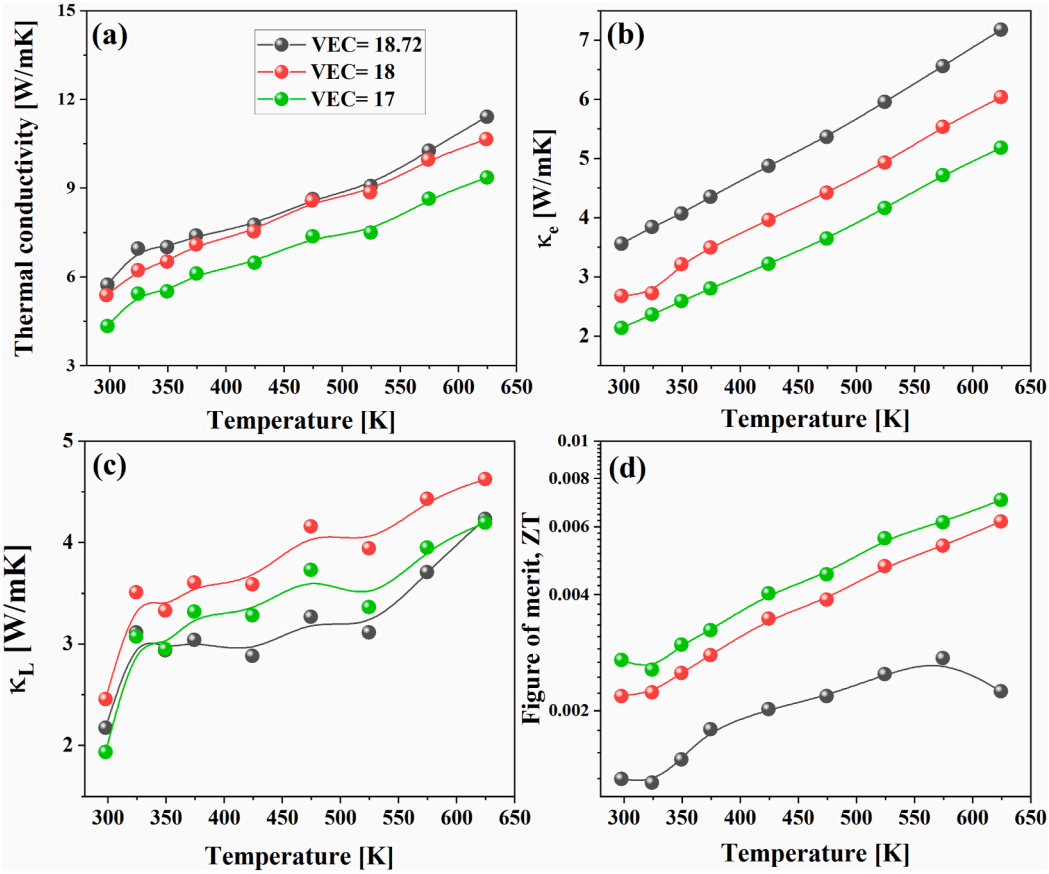

Fig. 6. Temperature-dependent (a) total thermal conductivity, (b) electronic thermal conductivity, (c) lattice thermal conductivity, and (d) ZT values for VEC (18.72, 18, and 17).

Declaration of competing interest

The authors declare that they have no known competing financial interests or personal relationships that could have appeared to influence the work reported in this paper.

Acknowledgments

We are grateful to Ole Bjørn Karlsen for helping with the initial sample preparation methodologies. We acknowledge the Research Council of Norway for financial support through the projects ANSWER Project No. 280545, NEAT project 262334, and NORFAB Project No.245963.

References

[1] L.-D. Zhao, V.P. Dravid, M.G. Kanatzidis, The panoscopic approach to high performance thermoelectrics, Energy Environ. Sci. 7 (1) (2014) 251–268.
[2] T.M. Tritt, M. Subramanian, Thermoelectric materials, phenomena, and applications: a bird's eye view, MRS Bull. 31 (2006) 188–198, 03.
[3] C. Kittel, Introduction to Solid State Physics, John Wiley & Sons, 2005.
[4] E. Flage-Larsen, O. Prytz, The Lorenz function: its properties at optimum thermoelectric figure-of-merit, Appl. Phys. Lett. 99 (20) (2011) 202108.
[5] H.-S. Kim, Z.M. Gibbs, Y. Tang, H. Wang, G.J. Snyder, Characterization of Lorenz number with Seebeck coefficient measurement, Apl. Mater. 3 (2015), 041506.
[6] J.U. Rahman, E.-J. Meang, D. Nguyen, W.-S. Seo, A. Hussain, M.H. Kim, S. Lee, The synthesis and thermoelectric properties of p-type $Li_{1-x}NbO_2$-based compounds, J. Electron. Mater. 3 (46) (2017) 1740–1746.
[7] B. Poudel, Q. Hao, Y. Ma, Y. Lan, A. Minnich, B. Yu, X. Yan, D. Wang, A. Muto, D. Vashaee, High-thermoelectric performance of nanostructured bismuth antimony telluride bulk alloys, Science 320 (5876) (2008) 634–638.
[8] M. Ibánez, Z. Luo, A. Genc, L. Piveteau, S. Ortega, D. Cadavid, O. Dobrozhan, Y. Liu, M. Nachtegaal, M. Zebarjadi, High-performance thermoelectric nanocomposites from nanocrystal building blocks, Nat. Commun. 7 (1) (2016) 1–7.
[9] J.M. Song, J.U. Rahman, J.Y. Cho, S. Lee, W.S. Seo, S. Kim, S.-i. Kim, K.H. Lee, D. Roh, W.H. Shin, Chemically synthesized Cu_2Te incorporated Bi-Sb-Te *p*-type thermoelectric materials for low temperature energy harvesting, Scripta Mater. 165 (2019) 78–83.
[10] T. Graf, C. Felser, S.S.P. Parkin, Simple rules for the understanding of Heusler compounds, Prog. Solid State Chem. 39 (1) (2011) 1–50.
[11] T. Graf, S.P.P. Parkin, C. Frelser, Heusler compounds—a material class with exceptional properties, IEEE Trans. Magn. 47 (2011) 367.
[12] C.J. Palmstrøm, Heusler compounds and spintronics, Prog. Cryst. Growth Char. Mater. 62 (2) (2016) 371–397.
[13] F. Casper, T. Graf, S. Chadov, B. Balke, C. Felser, Half-Heusler compounds: novel materials for energy and spintronic applications, Semicond. Sci. Technol. 27 (6) (2012).
[14] C. Fu, S. Bai, Y. Liu, Y. Tang, L. Chen, X. Zhao, T. Zhu, Realizing high figure of merit in heavy-band p-type half-Heusler thermoelectric materials, Nat. Commun. 6 (2015) 8144.
[15] H. Zhu, J. Mao, Y. Li, J. Sun, Y. Wang, Q. Zhu, G. Li, Q. Song, J. Zhou, Y. Fu, R. He, T. Tong, Z. Liu, W. Ren, L. You, Z. Wang, J. Luo, A. Sotnikov, J. Bao, K. Nielsch, G. Chen, D.J. Singh, Z. Ren, Discovery of TaFeSb-based half-Heuslers with high thermoelectric performance, Nat. Commun. 10 (1) (2019) 270.
[16] M. Schrade, K. Berland, A. Kosinskiy, J.P. Heremans, T.G. Finstad, Shallow impurity band in ZrNiSn, J. Appl. Phys. 127 (4) (2020).
[17] N. Van Du, J.U. Rahman, P.T. Huy, W.H. Shin, W.-S. Seo, M.H. Kim, S. Lee, X-site aliovalent substitution decoupled charge and phonon transports in XYZ half-Heusler thermoelectrics, Acta Mater. 166 (2019) 650–657.
[18] N. Van Du, J.U. Rahman, E.-J. Meang, C.-H. Lim, W.H. Shin, W.-S. Seo, P.T. Huy, M.H. Kim, S. Lee, Synthesis and thermoelectric properties of Ti-substituted (Hf0. 5Zr0. 5) 1-xTixNiSn0. 998Sb0. 002 Half-Heusler compounds, J. Alloys Compd. 773 (2019) 1141–1145.
[19] S. Poon, Recent advances in thermoelectric performance of half-heusler compounds, Metals 8 (12) (2018).
[20] S. Chadov, X. Qi, J. Kubler, G.H. Fecher, C. Felser, S.C. Zhang, Tunable multifunctional topological insulators in ternary Heusler compounds, Nat. Mater. 9 (7) (2010) 541–545.
[21] G. Ding, G.Y. Gao, L. Yu, Y. Ni, K. Yao, Thermoelectric properties of half-Heusler topological insulators MPtBi (M = Sc, Y, La) induced by strain, J. Appl. Phys. 119 (2) (2016).
[22] D. Kieven, R. Klenk, S. Naghavi, C. Felser, T. Gruhn, I-II-V half-Heusler compounds for optoelectronics:Ab initiocalculations, Phys. Rev. B 81 (7) (2010).

[23] S. Kacimi, H. Mehnane, A. Zaoui, I–II–V and I–III–IV half-Heusler compounds for optoelectronic applications: comparative ab initio study, J. Alloys Compd. 587 (2014) 451–458.

[24] F. Parvin, M.A. Hossain, I. Ahmed, K. Akter, A.K.M.A. Islam, First-principles calculations to investigate mechanical, optoelectronic and thermoelectric properties of half-Heusler p-type semiconductor BaAgP, Results Phys. 23 (2021).

[25] N. Belmiloud, F. Boutaiba, A. Belabbes, M. Ferhat, F. Bechstedt, Half-Heusler compounds with a 1 eV (1.7 eV) direct band gap, lattice-matched to GaAs (Si), for solar cell application: a first-principles study, Phys. Status Solidi 253 (5) (2016) 889–894.

[26] M. Schrade, K. Berland, S.N.H. Eliassen, M.N. Guzik, C. Echevarria-Bonet, M. H. Sorby, P. Jenus, B.C. Hauback, R. Tofan, A.E. Gunnaes, C. Persson, O.M. Lovvik, T.G. Finstad, The role of grain boundary scattering in reducing the thermal conductivity of polycrystalline XNiSn (X = Hf, Zr, Ti) half-Heusler alloys, Sci. Rep. 7 (1) (2017) 13760.

[27] Y. Liu, H. Xie, C. Fu, G.J. Snyder, X. Zhao, T. Zhu, Demonstration of a phonon-glass electron-crystal strategy in (Hf,Zr)NiSn half-Heusler thermoelectric materials by alloying, J. Mater. Chem. 3 (45) (2015) 22716–22722.

[28] S. Chen, K.C. Lukas, W. Liu, C.P. Opeil, G. Chen, Z. Ren, Effect of Hf concentration on thermoelectric properties of nanostructured N-type half-heusler materials HfxZr1-xNiSn0.99Sb0.01, Adv. Energy Mater. 3 (9) (2013) 1210–1214.

[29] D.B. Miracle, O.N. Senkov, A critical review of high entropy alloys and related concepts, Acta Mater. 122 (2017) 448–511.

[30] Y. Ye, Q. Wang, J. Lu, C. Liu, Y. Yang, High-entropy alloy: challenges and prospects, Mater. Today 19 (6) (2016) 349–362.

[31] Y. Lu, Y. Dong, S. Guo, L. Jiang, H. Kang, T. Wang, B. Wen, Z. Wang, J. Jie, Z. Cao, A promising new class of high-temperature alloys: eutectic high-entropy alloys, Sci. Rep. 4 (1) (2014) 1–5.

[32] P. Koželj, S. Vrtnik, A. Jelen, S. Jazbec, Z. Jagličić, S. Maiti, M. Feuerbacher, W. Steurer, J. Dolinšek, Discovery of a superconducting high-entropy alloy, Phys. Rev. Lett. 113 (10) (2014) 107001.

[33] L. Liu, J.B. Zhu, J.C. Li, Q. Jiang, Microstructure and magnetic properties of FeNiCuMnTiSnx high entropy alloys, Adv. Eng. Mater. 14 (10) (2012) 919–922.

[34] Y. Zhang, T.T. Zuo, Z. Tang, M.C. Gao, K.A. Dahmen, P.K. Liaw, Z.P. Lu, Microstructures and properties of high-entropy alloys, Prog. Mater. Sci. 61 (2014) 1–93.

[35] R. Valiev, Nanostructuring of metals by severe plastic deformation for advanced properties, Nat. Mater. 3 (8) (2004) 511–516.

[36] R.Z. Valiev, Y. Estrin, Z. Horita, T.G. Langdon, M.J. Zechetbauer, Y.T. Zhu, Producing bulk ultrafine-grained materials by severe plastic deformation, JOM (J. Occup. Med.) 58 (4) (2006) 33–39.

[37] Y. Luo, S. Hao, S. Cai, T.J. Slade, Z.Z. Luo, V.P. Dravid, C. Wolverton, Q. Yan, M. G. Kanatzidis, High thermoelectric performance in the new cubic semiconductor AgSnSbSe3 by high-entropy engineering, J. Am. Chem. Soc. 142 (35) (2020) 15187–15198.

[38] B. Jiang, Y. Yu, J. Cui, X. Liu, L. Xie, J. Liao, Q. Zhang, Y. Huang, S. Ning, B. Jia, High-entropy-stabilized chalcogenides with high thermoelectric performance, Science 371 (6531) (2021) 830–834.

[39] A. Karati, M. Nagini, S. Ghosh, R. Shabadi, K. Pradeep, R.C. Mallik, B. Murty, U. Varadaraju, Ti 2 NiCoSnSb-a new half-Heusler type high-entropy alloy showing simultaneous increase in Seebeck coefficient and electrical conductivity for thermoelectric applications, Sci. Rep. 9 (1) (2019) 1–12.

[40] D. Zhao, L. Wang, L. Bo, D. Wu, Synthesis and thermoelectric properties of Ni-doped ZrCoSb half-Heusler compounds, Metals 8 (1) (2018) 61.

[41] H. Hou, X. Cao, Y. Yang, L. Fang, C. Pan, X. Yang, W. Song, X. Ji, NiSb alloy hollow nanospheres as anode materials for rechargeable lithium ion batteries, Chem. Commun. 50 (60) (2014) 8201–8203.

[42] Q. Pan, Y. Wu, W. Zhong, F. Zheng, Y. Li, Y. Liu, J. Hu, C. Yang, Carbon nanosheets encapsulated NiSb nanoparticles as advanced anode materials for lithium-ion batteries, Energy Environ. Mater. 3 (2) (2020) 186–191.

[43] Y.-y. Qian, J. Yang, H.-r. Li, S.-q. Xing, Q. Yang, Solution-based synthesis of NiSb nanoparticles for electrochemical activity in hydrogen evolution reaction, Chin. J. Chem. Phys. 32 (3) (2019) 373.

[44] V.S. Marakatti, S.C. Peter, Nickel–antimony nanoparticles confined in SBA-15 as highly efficient catalysts for the hydrogenation of nitroarenes, New J. Chem. 40 (6) (2016) 5448–5457.

[45] D. Young, P. Khalifah, R.J. Cava, A. Ramirez, Thermoelectric properties of pure and doped FeMSb (M= V, Nb), J. Appl. Phys. 87 (1) (2000) 317–321.

[46] Y. Xia, S. Bhattacharya, V. Ponnambalam, A. Pope, S. Poon, T. Tritt, Thermoelectric properties of semimetallic (Zr, Hf) CoSb half-Heusler phases, J. Appl. Phys. 88 (4) (2000) 1952–1955.

[47] H. Kleinke, New bulk materials for thermoelectric power generation: clathrates and complex antimonides, Chem. Mater. 22 (3) (2010) 604–611.

[48] N. Kazem, S.M. Kauzlarich, Thermoelectric Properties of Zintl Antimonides, Handbook on the Physics and Chemistry of Rare Earths, Elsevier, 2016, pp. 177–208.

[49] B. Khan, H.R. Aliabad, I. Khan, S. Jalali-Asadabadi, I. Ahmad, Comparative study of thermoelectric properties of Co based filled antimonide skutterudites with and without SOC effect, Comput. Mater. Sci. 131 (2017) 308–314.

[50] B. Sales, D. Mandrus, R.K. Williams, Filled skutterudite antimonides: a new class of thermoelectric materials, Science 272 (5266) (1996) 1325–1328.

[51] K. Valset, X. Song, T. Finstad, A study of transport properties in Cu and P doped ZnSb, J. Appl. Phys. 117 (4) (2015), 045709.

[52] M. Schrade, H. Fjeld, T. Norby, T.G. Finstad, Versatile apparatus for thermoelectric characterization of oxides at high temperatures, Rev. Sci. Instrum. 85 (10) (2014) 103906.

[53] Y. Zhang, M. Gao, J. Yeh, P. Liaw, Y. Zhang, High-Entropy Alloys: Fundamentals and Applications, 2016.

[54] W. Zhang, P.K. Liaw, Y. Zhang, Science and technology in high-entropy alloys, Sci. China Mater. 61 (1) (2018) 2–22.

[55] R.-Z. Zhang, M.J. Reece, Review of high entropy ceramics: design, synthesis, structure and properties, J. Mater. Chem. 7 (39) (2019) 22148–22162.

[56] M.J. Otto, R.A.M. van Woerden, P.J. van der Valk, J. Wijngaard, C.F. van Bruggen, C. Haas, K.H.J. Buschow, Half-metallic ferromagnets: I. Structure and magnetic properties of NiMnSb and related inter-metallic compounds, J. Phys. Condens. Matter 1 (1989) 2341–2350.

[57] D. Orgassa, H. Fujiwara, T.C. Schulthess, W.H. Butler, First-principles calculation of the effect of atomic disorder on the electronic structure of the half-metallic ferromagnet NiMnSb, Phys. Rev. B 60 (1999) 13237.

[58] N. Zhao, A. Sud, H. Sukegawa, S. Komori, K. Rogdakis, K. Yamanoi, J. Patchett, J. W.A. Robinson, C. Ciccarelli, H. Kurebayashi, Growth, strain, and spin-orbit torques in epitaxial Ni-Mn-Sb films sputtered on GaAs, Phys. Rev. Mater. 5 (1) (2021).

[59] I.V. Chumak, V.V. Pavlyuk, G.S. Dmytriv, J. Sepien-Damm, Phase equilibria and crystal structure of compounds in the Fe–Zn–Sb system at 570 K, J. Alloys Compd. 307 (2000) 223–225.

[60] D.-B. Xiong, Y. Zhao, Half-Heusler phase related structural perturbations near stoichiometric composition FeZnSb, J. Solid State Chem. 184 (5) (2011) 1159–1164.

[61] K. Persson, Materials Data on ZnFeSb (SG:216) by Materials Project, United States, 2014.

[62] D.B. Xiong, N.L. Okamoto, T. Waki, Y. Zhao, K. Kishida, H. Inui, High-Tc ferromagnetic semiconductor-like behavior and unusual electrical properties in compounds with a 2x2x2 superstructure of the half-Heusler phase, Chemistry 18 (9) (2012) 2536–2542.

[63] K. Kutorasinski, J. Tobola, S. Kaprzyk, Application of Boltzmann transport theory to disordered thermoelectric materials: Ti (Fe, Co, Ni) Sb half-Heusler alloys, Phys. Status Solidi 211 (6) (2014) 1229–1234.

[64] V. Ksenofontov, G. Melnyk, M. Wojcik, S. Wurmehl, K. Kroth, S. Reiman, P. Blaha, C. Felser, Structure and properties of CoMnSb in the context of half-metallic ferromagnetism, Phys. Rev. B 74 (13) (2006) 134426.

[65] S. Kirklin, J.E. Saal, B. Meredig, A. Thompson, J.W. Doak, M. Aykol, S. Rühl, C. Wolverton, The Open Quantum Materials Database (OQMD): assessing the accuracy of DFT formation energies, NPJ Comput. Mater. 1 (2015) 15010.

[66] J.E. Saal, S. Kirklin, M. Aykol, B. Meredig, C. Wolverton, Materials design and discovery with high-throughput density functional theory: the open quantum materials database (OQMD), JOM (J. Occup. Med.) 65 (2013) 1501–1509.

[67] T.M. Tritt, Thermoelectric phenomena, materials, and applications, Annu. Rev. Mater. Res. 41 (2011) 433–448.

[68] J.U. Rahman, N. Van Du, W.H. Nam, W.H. Shin, K.H. Lee, W.-S. Seo, M.H. Kim, S. Lee, Grain boundary interfaces controlled by reduced graphene oxide in nonstoichiometric $SrTiO_{3-\delta}$ thermoelectrics, Sci. Rep. 9 (1) (2019) 1–12.